

Crystalline silicon solar cells with thin poly-SiO_x carrier-selective passivating contacts for perovskite/c-Si tandem applications

Singh, Manvika; Amarnath, Aswathy; Wagner, Fabian; Zhao, Yifeng; Yang, Guangtao; Mazzarella, Luana; Weeber, Arthur W.; Zeman, Miro; Isabella, Olindo; More Authors

DOI

[10.1002/pip.3693](https://doi.org/10.1002/pip.3693)

Publication date

2023

Document Version

Final published version

Published in

Progress in Photovoltaics: research and applications

Citation (APA)

Singh, M., Amarnath, A., Wagner, F., Zhao, Y., Yang, G., Mazzarella, L., Weeber, A. W., Zeman, M., Isabella, O., & More Authors (2023). Crystalline silicon solar cells with thin poly-SiO_x carrier-selective passivating contacts for perovskite/c-Si tandem applications. *Progress in Photovoltaics: research and applications*, 31(9), 877-887. <https://doi.org/10.1002/pip.3693>

Important note

To cite this publication, please use the final published version (if applicable).
Please check the document version above.

Copyright

Other than for strictly personal use, it is not permitted to download, forward or distribute the text or part of it, without the consent of the author(s) and/or copyright holder(s), unless the work is under an open content license such as Creative Commons.

Takedown policy

Please contact us and provide details if you believe this document breaches copyrights.
We will remove access to the work immediately and investigate your claim.

Crystalline silicon solar cells with thin poly-SiO_x carrier-selective passivating contacts for perovskite/c-Si tandem applications

Manvika Singh¹ | Kunal Datta² | Aswathy Amarnath¹ | Fabian Wagner¹ |
 Yifeng Zhao¹ | Guangtao Yang¹ | Andrea Bracesco² | Nga Phung² |
 Dong Zhang^{3,4} | Valerio Zardetto⁴ | Mehrdad Najafi⁴ | Sjoerd C. Veenstra⁴ |
 Gianluca Coletti^{5,6} | Luana Mazzarella¹ | Mariadriana Creatore² |
 Martijn M. Wienk³ | René A. J. Janssen^{2,3,7} | Arthur W. Weeber^{1,5} |
 Miro Zeman¹ | Olindo Isabella¹

¹PVMD Group, Delft University of Technology, Mekelweg 4, 2628 CD Delft, The Netherlands

²Department of Applied Physics and Science Education, Eindhoven University of Technology, P.O. Box 513, 5600 MB Eindhoven, The Netherlands

³Department of Chemical Engineering and Chemistry, Eindhoven University of Technology, P.O. Box 513, 5600 MB Eindhoven, The Netherlands

⁴TNO-partner in Solliance, High Tech Campus 21, 5656 AE Eindhoven, The Netherlands

⁵TNO Energy & Materials Transition, Westerduinweg 3, 1755 LE Petten, The Netherlands

⁶School of Photovoltaic and Renewable Energy Engineering, University of New South Wales, Sydney, Australia

⁷Dutch Institute for Fundamental Energy Research, De Zaal 20, 5612 AJ Eindhoven, The Netherlands

Correspondence

Manvika Singh, PVMD group, Delft University of Technology, Mekelweg 4, 2628 CD Delft, The Netherlands.

Email: m.singh-1@tudelft.nl

Funding information

Ministry of Economic Affairs and Climate Affairs, Grant/Award Numbers: 1921202, TEUE119005; SOLAR-ERA.NET Cofund; Netherlands Ministry of Economic Affairs and Climate Policy

Abstract

Single junction crystalline silicon (c-Si) solar cells are reaching their practical efficiency limit whereas perovskite/c-Si tandem solar cells have achieved efficiencies above the theoretical limit of single junction c-Si solar cells. Next to low-thermal budget silicon heterojunction architecture, high-thermal budget carrier-selective passivating contacts (CSPCs) based on polycrystalline-SiO_x (poly-SiO_x) also constitute a promising architecture for high efficiency perovskite/c-Si tandem solar cells. In this work, we present the development of c-Si bottom cells based on high temperature poly-SiO_x CSPCs and demonstrate novel high efficiency four-terminal (4T) and two-terminal (2T) perovskite/c-Si tandem solar cells. First, we tuned the ultra-thin, thermally grown SiO_x. Then we optimized the passivation properties of p-type and n-type doped poly-SiO_x CSPCs. Here, we have optimized the p-type doped poly-SiO_x CSPC on textured interfaces via a two-step annealing process. Finally, we integrated such bottom solar cells in both 4T and 2T tandems, achieving 28.1% and 23.2% conversion efficiency, respectively.

This is an open access article under the terms of the [Creative Commons Attribution](https://creativecommons.org/licenses/by/4.0/) License, which permits use, distribution and reproduction in any medium, provided the original work is properly cited.

© 2023 The Authors. Progress in Photovoltaics: Research and Applications published by John Wiley & Sons Ltd.

1 | INTRODUCTION

Single junction c-Si solar cells are reaching their practical efficiency limit.^{1,2} One way to further increase the efficiency of solar cells based on c-Si is to deploy them as bottom device in tandem structures with a wide bandgap top device. Perovskite/c-Si tandem solar cells attract considerable attention in this regard³⁻³¹ with certified conversion efficiencies so far up to 32.5%.³² The two common tandem architectures are a monolithically integrated two-terminal (2T) tandem configuration, where the two devices are electrically connected via a tunnel recombination junction (TRJ), and a mechanically stacked four-terminal (4T) tandem configuration where the two devices are optically connected but electrically decoupled. The 2T tandem solar cell design has simple electrical connections but requires current matching between the two devices to reach optimal efficiency. It is thus sensitive to the daily variations of solar spectrum. The 4T tandem configuration does not require current matching between its component devices and so has fewer restrictions on the device optimizations. However, due to the devices being electrically decoupled, each of them has its own transport layers and additional encapsulation layers for optical coupling, which increases the overall parasitic absorption. The advantages and disadvantages of 2T and 4T tandem configurations have been explored before.^{4,33-35} As bottom device, besides silicon heterojunction (SHJ) cells,^{3-7,24-27} silicon solar cells based on high-thermal budget carrier-selective passivating contacts (CSPCs) have rarely been reported.^{8,28-30} Such CSPCs are so-called because they require high temperature fabrication steps, which can be up to 1100°C. Polycrystalline silicon (poly-Si) is an example of these high-thermal budget CSPCs and has enabled high efficiency single junction c-Si solar cells,³⁶⁻⁴⁰ concurrently yielding high quality surface passivation and charges transport. However, doped poly-Si exhibits a high free carrier absorption, which has turned the attention of researchers towards wide bandgap materials, such as polycrystalline-SiC_x^{41,42} and polycrystalline-SiO_x (poly-SiO_x), which can be more transparent while ensuring similar conductivity with respect to poly-Si.^{43,44} Such CSPCs consist of doped poly-Si, alloyed with carbon or oxygen, which are deposited on an ultra-thin SiO_x layer, prepared by a wet-chemical process (nitric acid oxidation of silicon, NAOS),⁴⁴ thermal oxidation,⁴⁵ UV/O₃ process,⁴⁶ or low-temperature plasma oxidation.⁴⁷ The optoelectronic properties of poly-SiO_x depend on the oxygen content.^{44,48} Poly-SiO_x is a novel material that has been successfully employed in c-Si single junction solar cells^{44,48,49} and, to the best of our knowledge, its long-wavelength optical potential in tandems has not been explored so far. As these CSPCs are compatible with high temperature production processes, they are appealing to the mainstream c-Si PV industry. In view of potential tandem efficiencies well above 30%, perovskite/c-Si tandem solar cells with bottom cells fabricated with high-thermal budget CSPCs can significantly reduce the levelized cost of electricity compared to single junction silicon photovoltaics.⁵⁰

Solar cells fabricated with poly-SiO_x CSPCs on an ultra-thin tunnelling SiO_x layer grown via NAOS process have exhibited active area efficiency of around 21% in a front/back contacted (FBC) architecture.⁴⁹ However, these cells were 2-cm² wide and deployed

thermally evaporated metal contacts. In this work, next to adopting screen printing for metallization and developing larger area devices (from 2 to 4 cm²), an ultra-thin SiO_x layer prepared by thermal oxidation of the c-Si surface is used as tunnelling SiO_x. As compared with tunnelling oxide grown via NAOS, thermal oxides are denser and less prone to blistering, have lesser bulk defects, provide better wafer chemical passivation,⁵¹ and are more stoichiometric resulting in higher thermal stability.⁵² Other advantages of using a thermal oxide are (i) the controllability over the oxide thickness and its microstructures by changing the oxygen flow rate, temperature, and time and (ii) the industrial applicability in state-of-the-art furnaces.

We optimized the passivation of both n-type and p-type doped poly-SiO_x on the ultra-thin thermally grown SiO_x especially because p-type poly-SiO_x on textured surfaces has been a limiting factor in terms of passivation.^{42,51,53} To this end, a two-step annealing process was used to improve the passivation quality of p-type poly-SiO_x CSPCs on textured interfaces. Finally, we studied the integration of c-Si solar cells endowed with these optimized high-thermal budget CSPCs in perovskite/c-Si 4T and 2T tandem devices, achieving conversion efficiency of 28.07% and 23.18%, respectively.

2 | EXPERIMENTAL DETAILS

2.1 | Crystalline silicon (c-Si) solar cells

We used 4-in. n-type float zone (FZ) double-side polished (DSP) Topsis wafers (orientation: <100>, resistivity: 1–5 Ω cm, thickness: 280 ± 20 μm). For double-side textured (DST) solar cells, both sides of the wafers were textured in a tetramethylammonium hydroxide (TMAH) solution containing ALKA-TEX (GP-Solar-GmbH) as additive. For single-side textured (SST) solar cells, the front side was protected by a thick silicon dioxide (SiO₂) layer deposited using plasma-enhanced chemical vapor deposition (PECVD). After partially texturing the wafer, the SiO₂ layer was etched using a buffered hydrogen fluoride (BHF [1:7]) solution. Subsequently, the samples were cleaned by dipping them in HNO₃ (99%), to remove eventual organic contaminations, and then in HNO₃ (69.5%, at 110°C) to remove inorganic contaminations. The samples are then dipped in 0.55% HF solution to remove any native oxide layer before thermal oxidation to grow a thin tunnelling oxide layer. Here, after preliminarily investigating an optimal growth temperature (ultimately fixed at 675°C), the time of the thermal oxidation process is optimized. Then, both the n-type and the p-type poly-SiO_x passivating contacts are deposited on the thermal oxide with a dual-stack layer of 10-nm thick intrinsic a-Si layer using low-pressure chemical vapor deposition (LPCVD) process and 20-nm thick doped a-SiO_x:H layer from the PECVD process. Silane (SiH₄), carbon dioxide (CO₂), and hydrogen (H₂) gases are used as the sources to deposit these poly-SiO_x passivating contacts. Phosphine (PH₃) and diborane (B₂H₆) gases are used as doping sources for n-type and p-type poly-SiO_x passivating contacts, respectively.⁴⁸ The dopant concentration of such poly-SiO_x CSPCs is in the order of 10²⁰ cm⁻³.^{43,48} The total thickness of the passivating contact hereby described will

not overcome 30 nm. Because of that thickness, an additional transparent conductive oxide (TCO) layer is needed for lateral transport of carriers. Also here, after an initial study on the optimal annealing temperature seeking for an eventual co-annealing temperature between the n-type and p-type doped layers, these samples were annealed at 950°C between 5 and 15 min to crystallize the abovementioned films into poly-SiO_x layers and drive in the dopants for both DST and SST cells. In this high temperature process, hydrogen effuses from the whole layer stack. Therefore, these cell precursors were hydrogenated by forming gas annealing (FGA) at 400°C for 1 h after being preliminarily capped with a 100-nm thick PECVD SiN_x layer.⁵⁴ Upon the removal of the SiN_x capping layer, indium tin oxide (ITO) layers were sputtered to ensure efficient (i) lateral carrier transport of charge carriers and (ii) optical performance at the front side as an anti-reflective coating (75 nm) and at the rear side as an optical buffer for the rear reflector (150 nm).⁵⁵ As this step deteriorates the passivation quality,^{49,56,57} an additional annealing was executed in hydrogen for 1 h at 400°C. Finally, screen printing and curing for 30 min at 170°C was used to realize low-temperature front and rear Ag-based metallic contacts. We have also fabricated a front side flat (rear side textured) c-Si solar cell that is deployed in 2T tandem devices (see Figure 1). The fabrication of such an architecture is described in more detail in Section 2.2. The current–voltage measurements of c-Si solar cells were performed using an AAA class Wacom WXS-90S-L2 solar simulator. The best SST and DST devices were certified at the CalTeC of the Institute for Solar Energy Research Hamelin (ISFH), Germany, which provided also the related external quantum efficiency (EQE)

spectra (illumination in-between the front metal fingers). For passivation tests, symmetrical samples were fabricated with n-type or p-type doped poly-SiO_x CSPCs on flat and textured c-Si wafers. A lifetime tester (Sinton WCT-120) was used to perform passivation measurements, such as implied open-circuit voltage (iV_{oc}), on precursors in quasi-steady-state photoconductance (QSSPC) or transient photoconductance decay (transient PCD) mode.^{58,59}

2.2 | Perovskite/c-Si tandem solar cells

For 2T perovskite/c-Si tandem solar cells, SST solar cells were fabricated with front side flat n-type poly-SiO_x and rear side textured p-type poly-SiO_x. This configuration of the bottom sub-cell is chosen to meet the requirements for depositing the perovskite top device in a p-i-n configuration. After high temperature annealing (900°C for 15 min) and the abovementioned hydrogenation step, the SiN_x capping layer was removed. This was followed by sputtering 30-nm (150-nm) thick ITO layer on the front (rear) side of the cell. Finally, a 500-nm thick Ag layer was deposited on the rear side of the cell using thermal evaporation. Atomic layer deposition (ALD), in combination with solution processing, thermal evaporation, and sputtering were used to fabricate the perovskite top device. On the front, flat ITO layer of the bottom device, the perovskite top device comprised in a bottom-up sequence NiO_x/2-(9H-carbazol-9-yl)ethyl]phosphonic acid (2PACz)/perovskite (1.67 eV)/C₆₀/SnO_x/ITO/MgF₂. The front electrical contact was made of evaporated silver. The 8-nm thick NiO_x layer

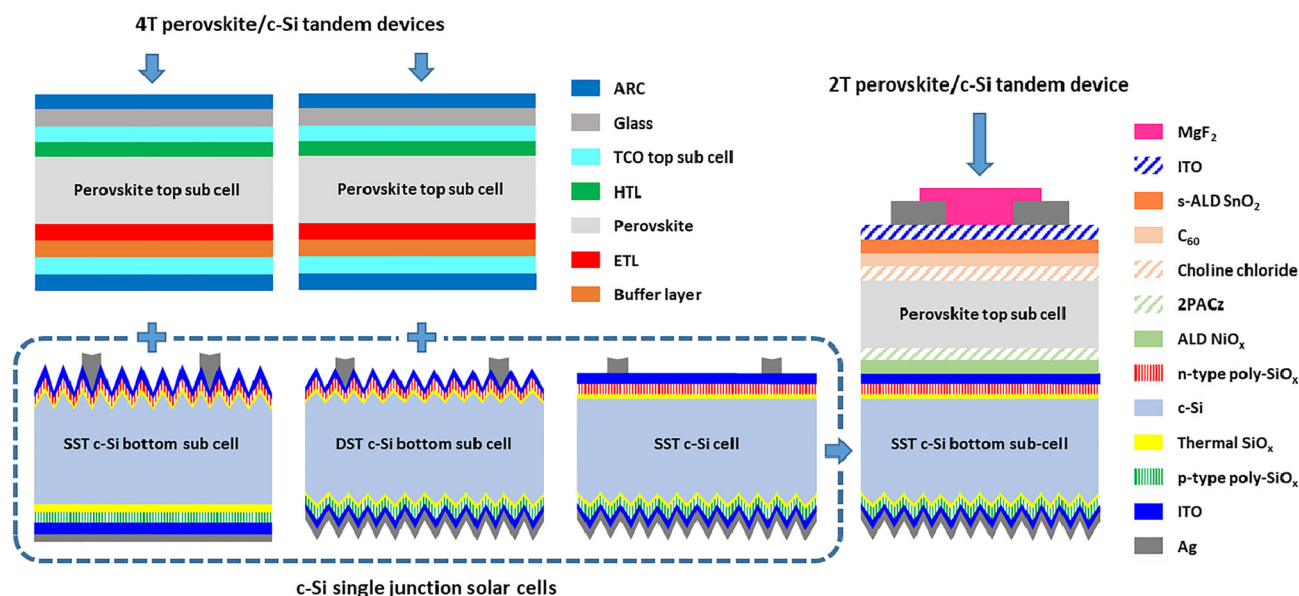


FIGURE 1 Sketches of the various solar cells reported in this work. The c-Si single junction solar cells endowed with p-type and n-type poly-SiO_x carrier-selective passivating contacts (CSPCs) are shown in the dashed box at the bottom left. The perovskite top cell is shown at top left. The abbreviations used are anti-reflection coating (ARC), transparent conductive oxide (TCO), hole transporting layer (HTL) and electron transporting layer (ETL). The single-side textured (SST) with front textured and the double-side textured (DST) solar cells are then combined with perovskite top cell to form 4T perovskite/c-Si tandem devices. The SST with rear textured solar cell is used for the 2T perovskite/c-Si tandem device. The indium tin oxide (ITO) layers of top and bottom cells in the 2T perovskite/c-Si tandem are processed in different labs on different layers, for which some differences in both optical and electrical properties are expected. [Colour figure can be viewed at [wileyonlinelibrary.com](https://onlinelibrary.wiley.com)]

was deposited on the ITO layer using thermal ALD.^{60,61} The deposition was done at a base pressure of 5×10^{-6} mbar in a home-built reactor using nickel bis(*N,N'*-di-*tert*-butylacetamidate) ($\text{Ni}(\text{tBu-MeAMD})_2$) as nickel precursor and water as the co-reactant. The precursor bubbler was maintained at 90°C, and an Ar flow was used for bubbling. The substrate temperature approached 150°C during the deposition. Subsequent solution-processed and evaporated layers were processed in an inert atmosphere. 2PACz (TCI, 98%, dissolved 0.3 mg/mL in ethanol) was deposited by spin coating at 3000 rpm for 30 s followed by annealing the substrate at 100°C for 10 min.⁶² The perovskite precursor solution was prepared by mixing 936 μL PbI_2 (TCI, >99.99%, 691.5 mg/mL in DMF:DMSO 4:1) with formamidinium iodide (FAI, Greatcell Solar Materials) (199.9 mg) and 936 μL PbBr_2 (TCI, >99%, 550.5 mg/mL in DMF:DMSO 4:1) with methylammonium bromide (MABr, Greatcell Solar Materials) (133.1 mg), followed by mixing the FAPbI_3 and MAPbBr_3 solutions in a 79:21 (v/v) ratio and adding 5 vol.% CsI (Sigma Aldrich, 99.999%, dissolved 389.7 mg/mL in DMSO) and 5 vol.% KI (Alfa Aesar, 99.998%, dissolved 249.0 mg/mL in DMF:DMSO 4:1). The precursor was spin-coated at 4000 rpm (5 s to reach 4000 rpm) for 35 s; at 25 s from the start of spin coating, 300 μL anisole was cast onto the substrate leading to perovskite crystallization. The substrate was then placed on a hot-plate, and the film was annealed at 100°C for 30 min. Following the substrate cooling down, choline chloride (Sigma Aldrich, >99%, 1 mg/mL in 2-propanol) was dynamically spin-coated at 4000 rpm for 35 s followed by thermal annealing at 100°C for 30 min. Then, C_{60} (10 nm) was deposited by thermal evaporation at a rate of 0.5 $\text{\AA}/\text{s}$. Following that, spatial atomic layer deposition (s-ALD) was used to deposit a SnO_2 (20 nm) buffer layer.⁶³ Tetrakis(dimethylamino)tin(IV) was used as tin precursor and water as the co-reactant. A nitrogen curtain was used to isolate the two half-reaction steps. A 180-nm thick ITO layer was deposited using Radio Frequency (RF) sputtering process at a rate of 0.3 $\text{\AA}/\text{s}$. Finally, a 100-nm thick Ag perimeter contact and a 120-nm thick MgF_2 anti-reflective coating were thermally evaporated to complete the tandem device. More information about this solar cell stack can be found in the research thesis of Kunal Datta.⁶⁴ Schematic sketches of single junction solar cells combined with perovskite solar cells in 4T and 2T tandem devices are reported in Figure 1.

Current density–voltage (J–V) scans of the 2T perovskite/*c*-Si tandem solar cells were done using a tungsten-halogen illumination source filtered by a UV filter (Schott GG385) and a daylight filter (Hoya LB120) with intensity adjusted to 100 mW/cm^2 . A 1- cm^2 shadow mask was used. The solar cells were operated under reverse or forward sweeps (between +2.0 V and –0.5 V for tandem solar cells) at a rate of 0.25 V/s using a Keithley 2400 source meter. The EQE measurements of the 2T perovskite/*c*-Si tandem solar cells were performed using a modulated monochromatic probe light (Philips focusline, 50 W) through a 1-mm radius aperture. The response was recorded and converted to the EQE using a calibrated silicon reference cell. Light- and voltage-biasing was used to isolate the EQE of the individual devices; 530 nm (perovskite) or 940 nm (silicon) bias light and a forward bias close to the open-circuit voltage of the single junction solar cell were used.

The single junction *c*-Si solar cells, described in Section 2.1, were combined with earlier processed and certified semi-transparent perovskite solar cells^{65–68} to fabricate the 4T tandem devices. The efficiency of 4T tandem cells was determined by following the procedure described by Werner et al.⁶⁹ Next to the conversion efficiency of our 4T tandem devices, another outcome of this procedure was the filtered EQE of the deployed bottom devices.

3 | RESULTS AND DISCUSSION

3.1 | Passivation properties of poly- SiO_x CSPCs

Here, we optimized the passivation quality of n-type and p-type doped poly- SiO_x CSPCs. Because SST poly- SiO_x passivated *c*-Si solar cell has n-type doped poly- SiO_x CSPC applied on front textured interface and p-type doped poly- SiO_x applied on rear side flat interface, we optimized n-type doped poly- SiO_x CSPC on DST symmetric samples and p-type doped poly- SiO_x on DSP symmetric samples (see Figure 2a). On the other hand, for DST poly- SiO_x passivated *c*-Si solar cell, we optimize both n-type and p-type doped poly- SiO_x CSPC applied on DST symmetric samples (see Figure 2b). As mentioned earlier in Section 2.1, these CSPCs are prepared stacking doped poly- SiO_x layers on a tunnelling oxide grown by thermal oxidation on a *c*-Si FZ wafer, followed by a high temperature annealing step. The passivation results in Figure 3 were obtained after the high temperature annealing step. We use two parameters to optimize the passivation of these CSPCs: (1) the thermal oxidation time for the growth of tunnelling oxide and (2) the annealing time. Figure 3a,b shows the passivation (in terms of iV_{oc}) of p-type doped poly- SiO_x CSPC applied on DSP symmetrical sample and n-type doped poly- SiO_x applied on DST symmetrical sample, respectively, for different thermal oxidation time at 675°C (shown with different colors). Three annealing times (5, 10, and 15 min at 950°C) were considered for each thermal oxidation time. For both p-type doped CSPC on DSP wafers and n-type doped poly- SiO_x CSPC on DST wafers, we found the same optimal thermal conditions for the tunnelling SiO_x and the high temperature annealing: 6 min at 675°C and 10 min at 950°C, respectively (see Figure 3a for p-type case and Figure 3b for n-type case).

On the other hand, for the symmetric p-type doped poly- SiO_x on DST wafer, notwithstanding the optimum found again at 10 min of thermal annealing in Figure 3c, thermally grown tunnelling SiO_x prepared at 675°C for 3 min was found to yield better results (iV_{oc} ~640 mV) than the rest of the samples. The underwhelming passivation performance of these DST samples can be ascribed to a strong Auger recombination due to the excessive diffusion of dopants in the *c*-Si bulk. To quench such a diffusion, a two-step annealing was used.^{70,71}

The first annealing step, done after the intrinsic a-Si layer deposition, was performed at 950°C for 1 min. This was meant to render this intrinsic silicon denser⁷² and therefore harder for dopants to be crossed. The second annealing step, done after the deposition of the doped a- SiO_x :H layer, was performed at 950°C between 5 and 15 min

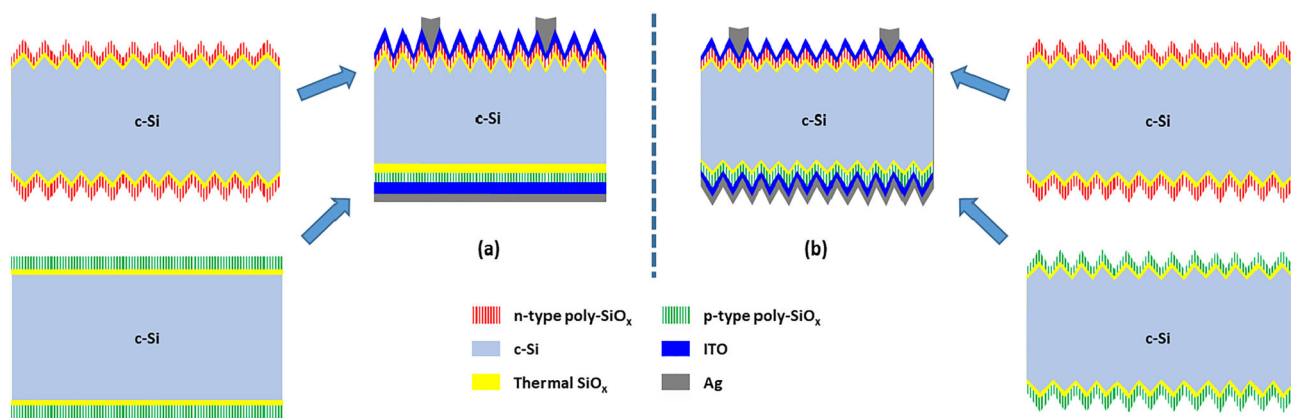
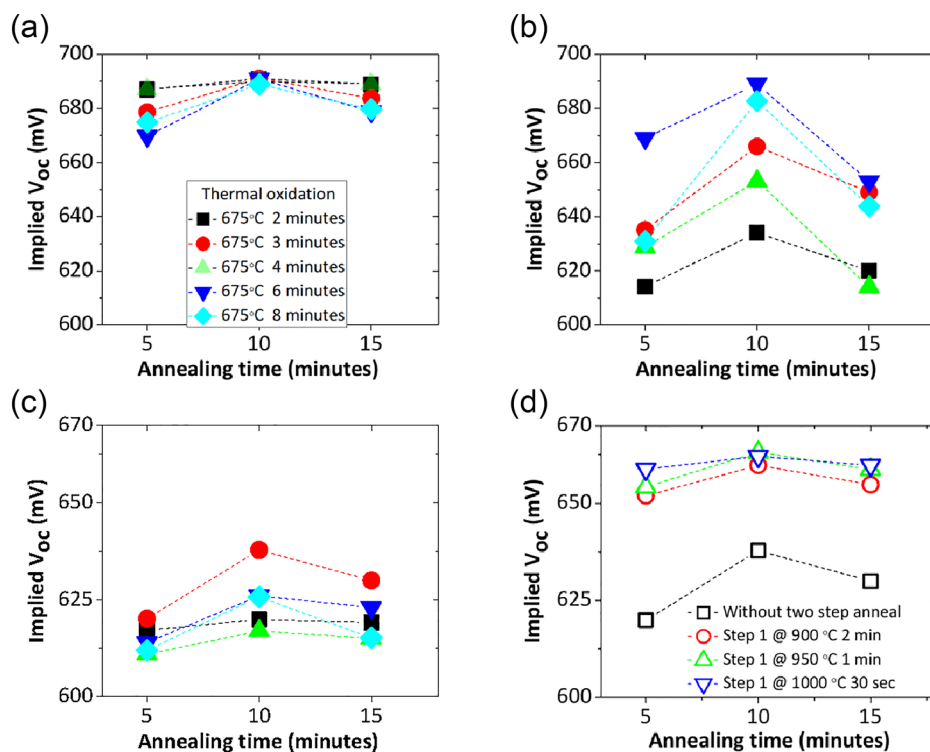


FIGURE 2 (a) Single-side textured (SST) poly-SiO_x passivated c-Si solar cell with (top) symmetric n-type doped poly-SiO_x on double-side textured (DST) substrate and (bottom) symmetric p-type doped poly-SiO_x double-side polished (DSP) substrate; (b) DST poly-SiO_x passivated c-Si solar cell with symmetric (top) n-type doped poly-SiO_x and (bottom) p-type doped poly-SiO_x on DST substrates. ITO, indium tin oxide. [Colour figure can be viewed at wileyonlinelibrary.com]

FIGURE 3 Implied V_{oc} of symmetric (a) p-type doped poly-SiO_x on double-side polished (DSP) wafer, (b) n-type doped poly-SiO_x on double-side textured (DST) wafer, and (c) p-type doped poly-SiO_x on DST wafer for different thermal oxidation times (thermal oxidation temperature is fixed at 675°C) and three annealing times (annealing temperature is fixed at 950°C). These three diagrams share the same legend. (d) Implied V_{oc} of symmetric p-type doped poly-SiO_x on DST wafer with two-step annealing. In this case, the thermal oxidation temperature and time are fixed at 675°C for 3 min. Here, the first step annealing temperature and time have been varied. For each first step annealing condition, a second step annealing time of 5, 10, and 15 min is considered, again at fixed annealing temperature (950°C). [Colour figure can be viewed at wileyonlinelibrary.com]



like in previous cases so far discussed. For this new series of samples, thermally grown tunnelling SiO_x was prepared at 675°C for 3 min. The passivation results for the symmetric p-type doped poly-SiO_x on DST wafers are reported in Figure 3d, showing more than 20 mV improvement with respect to the best passivation achieved with the single-step annealing.

As described in Section 2.1, hydrogenation by FGA after SiN_x layer capping is performed on p-type and n-type doped CSPCs to reintroduce the hydrogen that effused after high temperature annealing. Figure 4 shows the comparison in passivation of p-type and n-type doped poly-SiO_x symmetric samples after thermal annealing and

after hydrogenation. The optimum thermal oxidation and annealing conditions, as described in Figure 3, have been chosen for each type of CSPC. We observe that p-type and n-type doped poly-SiO_x CSPCs applied on DSP and DST symmetric samples, respectively, gave the same iV_{oc} of 690 mV after high temperature annealing, which improved to 710 mV after hydrogenation. The p-type poly-SiO_x symmetric sample without two-step annealing gave an iV_{oc} of 668 mV after hydrogenation. Using the two-step annealing technique, the symmetric p-type doped poly-SiO_x applied on DST wafer exhibited an iV_{oc} of 687 mV after hydrogenation. Applying the same two-step annealing technique to symmetric n-type doped poly-SiO_x on DST

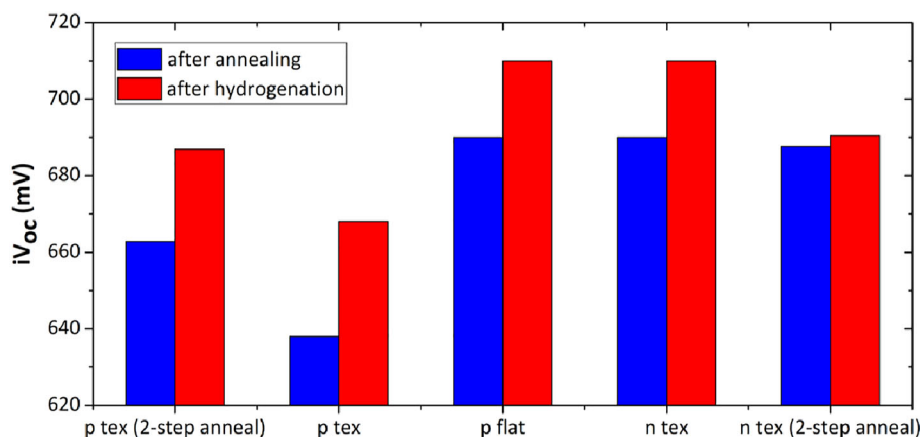


FIGURE 4 Implied V_{oc} for different types of carrier-selective passivating contacts (CSPCs) after high temperature annealing and after hydrogenation processes. Here, *tex* is used to denote textured. [Colour figure can be viewed at wileyonlinelibrary.com]

wafer (including the thermally grown tunnelling SiO_x prepared at 675°C for 3 min as in the p-type case), an iV_{oc} of 690 mV was found after hydrogenation, resulting in lower passivation quality than the single-step annealing case. Here, as the intrinsic poly-Si layer resulting from the first annealing got denser,⁷² we speculate that the phosphorus doping atoms do not easily reach the tunnelling SiO_x /c-Si bulk interface to establish an effective electric field. In addition, as shown in Figure 3b, the tunnelling SiO_x prepared at 675°C for 3 min is not the best condition for the n-type doped poly- SiO_x on a textured surface. Still, this case is investigated (and later put forward in solar cell fabrication) to realize a neat flow chart in which both n-type and p-type doped poly- SiO_x layers essentially undergo the same thermal processes at the same time.

3.2 | Solar cell results

In this section, we report on the performance of single junction c-Si solar cells with based on n-type and p-type poly- SiO_x as CSPCs. The sketches of SST and DST poly- SiO_x passivated c-Si solar cell were shown in Figure 2. The evolution of surface passivation quality after annealing, hydrogenation, TCO deposition, and hydrogen annealing for SST solar cell precursors is shown in Figure 5a. As expected, the iV_{oc} increases by 20 mV after hydrogenation. Then, the TCO deposition results in a considerable loss in iV_{oc} from 714 to 690 mV due to sputtering-related damages.^{49,57} This loss in passivation is recovered by annealing the cell precursor at 400°C in hydrogen environment for 1 h.⁵⁶ The best SST solar cell exhibited a certified designated area power conversion efficiency (PCE) of 20.47% ($V_{oc} = 695$ mV, $J_{sc} = 36.68$ mA/cm², FF = 80.33%, metallization fraction ~3%, designated area = 3.915 cm², see Figure 5c). Moving from the previous 2-cm² wide area device, SiO_x layer grown via wet-chemical NAOS and evaporated metallic contacts,⁴⁹ as well as applying the further optimized doped poly- SiO_x layers, we could keep the V_{oc} relatively high (from 691 to 695 mV) and sensibly improve the FF (from 76.4% to 80.3%) of the solar cells based on poly- SiO_x CSPCs.

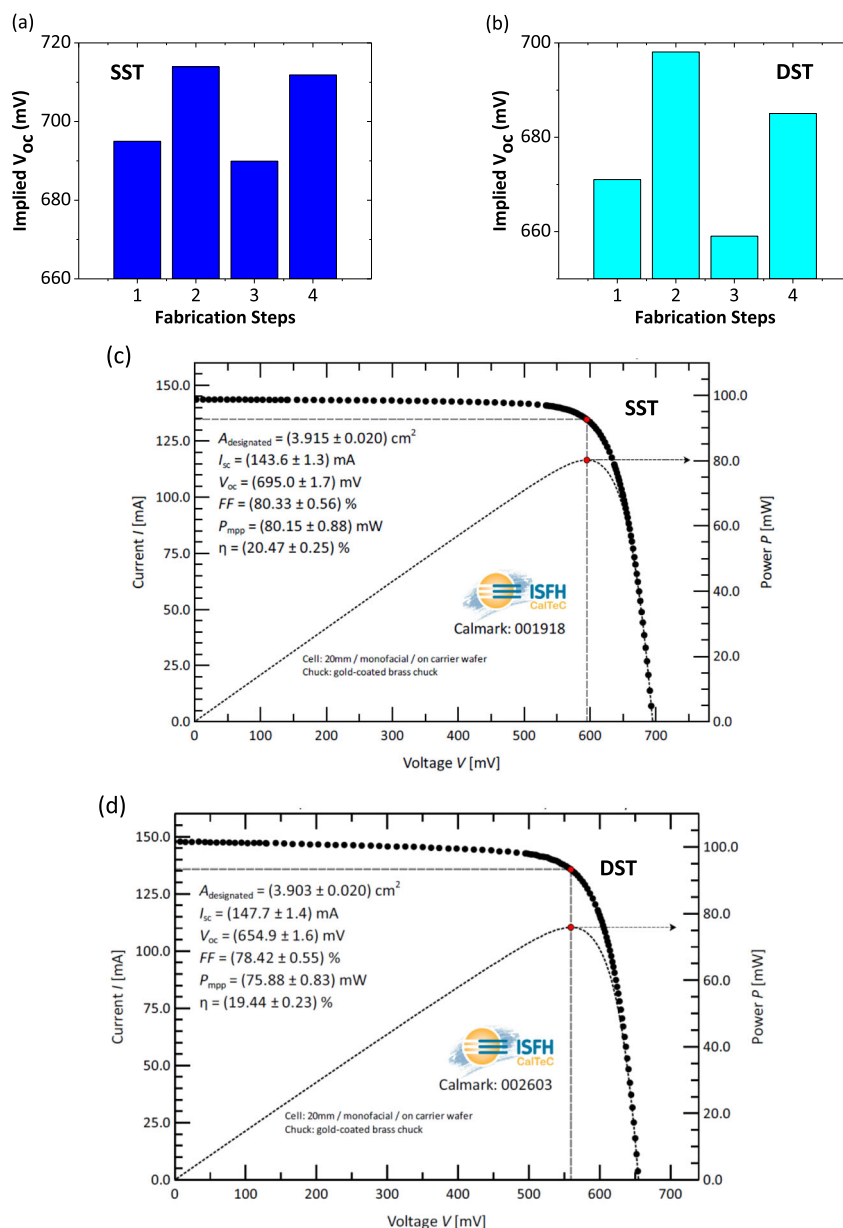
As mentioned in Section 3.1, the p-type and n-type doped poly- SiO_x CSPCs with two-step annealing technique are used as the hole

and electron contacts in DST solar cells, respectively. The change in passivation after different fabrication steps for the DST solar cell precursor is shown in Figure 5b. The increase in passivation after hydrogenation and its decrease after ITO deposition are as expected. However, unlike the SST case, the loss in passivation after TCO deposition is not fully recovered after hydrogen annealing at 400°C for 1 h. This is because the DST solar cell precursor has p-type doped CSPC applied to the textured side, which is the limiting factor in terms of passivation and does not recover its passivation even after such a hydrogen annealing. The best DST solar cell gave a certified designated area PCE of 19.44% ($V_{oc} = 655$ mV, $J_{sc} = 37.85$ mA/cm², FF = 78.42%, metallization fraction ~3%, designated area = 3.903 cm², see Figure 5d). Compared with the SST solar cell, despite suffering from poorer surface passivation as witnessed by the lower V_{oc} and FF, the DST cell exhibits higher J_{sc} . This gain can be ascribed to the textured rear side of the DST solar cell, which promotes a more efficient light scattering at the rear side and thus higher absorption in the c-Si bulk. Figure 6a shows the EQE of the SST and DST devices. As expected, the EQE of the DST cell outperforms that of the SST cell at wavelengths above 800 nm.

3.3 | Application in four-terminal (4T) perovskite/c-Si tandem solar cells

The SST and DST poly- SiO_x solar cells were deployed as bottom devices in high efficiency 4T tandem devices together with a previously processed and certified perovskite top device (bandgap 1.60 eV).^{65–68} The schematic sketches of the two 4T tandem devices alongside their constituting layers are presented in Figure 1. Following the method of measurement reported by Werner et al.⁶⁹ and with the certified measurements of both semi-transparent perovskite top and c-Si bottom devices, the combined results are summarized in Table 1. The 4T tandem devices based on SST and DST poly- SiO_x bottom devices provide a PCE of 27.97% and 28.07%, respectively. Both SST and DST cells, after being illuminated with the transmitted light through the perovskite top device, experienced similar J_{sc} losses. Looking at the filtered EQE (see Figure 6b), the DST cell keeps the

FIGURE 5 (a–b) The evolution in passivation quality (V_{oc}) after specific steps of single-side textured (SST) and double-side textured (DST) solar cell fabrication: (1) annealing, (2) hydrogenation, (3) Transparent conductive oxide (TCO) deposition, and (4) hydrogen annealing; (c–d) certified current–voltage and power–voltage curves of the best SST and DST poly-SiO_x passivated c-Si solar cell. Sketches of SST and DST solar cells are reported in Figure 2. [Colour figure can be viewed at [wileyonlinelibrary.com](https://onlinelibrary.wiley.com)]



optical edge over the SST cell for every wavelength above 800 nm. The SST cell loses however more in V_{oc} and FF than the DST cell. In fact, due to stronger Auger recombination at the p-type poly-SiO_x/tunnelling SiO_x/c-Si wafer side, the DST cell had poorer V_{oc} , which is less sensitive to light-induced carriers' injection, and FF more dominated by the low contact resistivity of the doped stack rather than an efficient extraction of light-induced majority carriers.

3.4 | Application in two-terminal (2T) perovskite/c-Si tandem solar cells

As sketched in Figure 1, we also fabricated SST solar cells with flat front side coated with n-type poly-SiO_x and textured rear side coated with p-type poly-SiO_x. This solar cell architecture was deployed to

form a 2T perovskite/c-Si tandem device with a p-i-n perovskite top device. Due to the textured p-type poly-SiO_x CSPC limiting the passivation quality, these solar cells suffered large passivation loss after the ITO deposition. Again, some of the passivation loss was recovered after annealing in hydrogen at 400°C for 1 h. The best single junction solar cell achieved a designated area PCE of 16.67% ($V_{oc} = 649 \text{ mV}$, $J_{sc} = 34.28 \text{ mA/cm}^2$, $FF = 74.93\%$, metallization fraction 3.15%, designated area = 3.92 cm^2). The current density–voltage characteristic and the EQE spectrum of the single junction solar cell are reported in Figure 7a,b, respectively. From the EQE and reflectance spectra in Figure 7b, we note large parasitic absorption at short wavelengths (300–400 nm) and at very long wavelengths (1000–1200 nm). This light is absorbed in the front/rear ITO and in the front/rear poly-SiO_x CSPCs. Between 600 and 1000 nm, other than the reflection losses, most of the light is absorbed in c-Si solar cell.

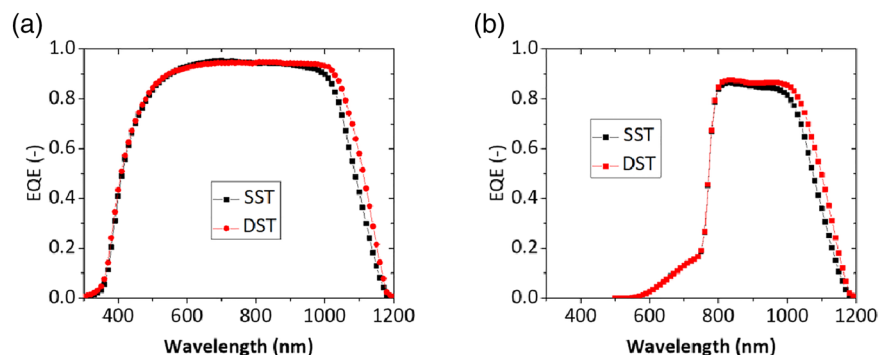


FIGURE 6 (a) External quantum efficiency (EQE) spectra of the single-side textured (SST) and double-side textured (DST) single junction c-Si solar cells endowed with n-type and p-type poly-SiO_x carrier-selective passivating contacts (CSPCs). (b) Filtered EQE spectra of the same solar cells deployed as bottom devices in 4T perovskite/c-Si tandem devices. [Colour figure can be viewed at wileyonlinelibrary.com]

TABLE 1 External parameters of the semi-transparent perovskite top device (certified at ESTI, code XF812), the SST poly-SiO_x bottom cell (certified at ISFH CalTeC, code 0019018), and DST poly-SiO_x bottom cell (certified at ISFH CalTeC, code 002603), and their 4T perovskite/c-Si tandem device combinations.

Solar cell	Description	V _{oc} (mV)	J _{sc} (mA/cm ²)	FF (%)	PCE (%)
Perovskite top device	Single junction	1139	22.00	78.60	19.70
SST poly-SiO _x -based bottom device	Single junction	695	36.68	80.33	20.47
	Filtered	666	16.00	77.60	8.27
	4T Tandem				27.97
DST poly-SiO _x -based bottom device	Single junction	655	37.85	78.42	19.44
	Filtered	637	16.80	78.20	8.37
	4T Tandem				28.07

Abbreviations: DST, double-side textured; PCE, power conversion efficiency; SST, single-side textured. The efficiencies of the 4T tandem are obtained by adding efficiencies of single junction c-Si and filtered perovskite top cell.

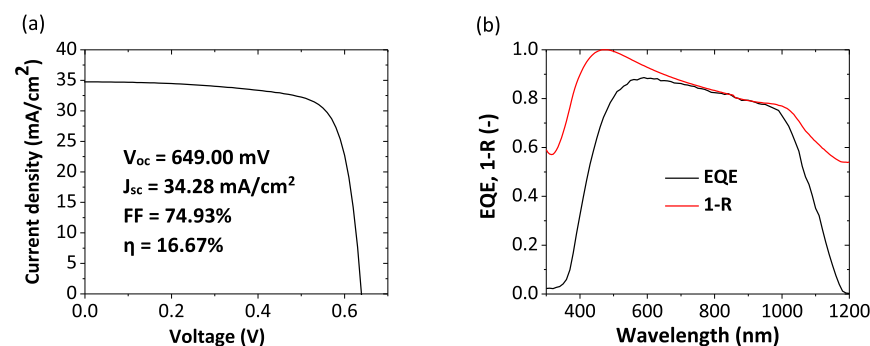


FIGURE 7 (a) Current density–voltage characteristic and (b) external quantum efficiency (EQE) and 1-Reflectance (1-R) spectra of the single junction c-Si solar cell with front side flat n-type poly-SiO_x and rear side textured p-type poly-SiO_x. The schematic of the corresponding structure is given in Figure 1. [Colour figure can be viewed at wileyonlinelibrary.com]

The abovementioned poly-SiO_x passivated c-Si solar cell was integrated with the perovskite top device into a 2T perovskite/c-Si tandem device yielding an active area PCE of 23.18% (V_{oc} = 1.76 V, J_{sc} = 17.8 mA/cm², FF = 74%, active area: 1 cm², see Figure 8a). The 2T tandem efficiency is higher than the efficiency of its top device by 5%_{abs} (with respect to an opaque analogous single junction perovskite solar cell efficiency^{64,73}) and the efficiency of its bottom device by 6.5%_{abs}. This efficiency is higher than that of the earlier reported value of 21.3% for a monolithic 2T perovskite/PERC-POLO tandem device (perovskite/silicon tandem featuring polycrystalline silicon on oxide (POLO) front junction and a passivated emitter and rearcell (PERC)-type passivated rear side with local aluminium p⁺ contacts).²⁹ On the other hand, it is

lower than that of the earlier reported value of 25.1% for monolithic 2T perovskite/c-Si tandem device where the bottom device is endowed with poly-SiC_x CSPCs.⁴² These three types of high-thermal budget devices exhibit similar V_{oc}s (1.74 to 1.8 V) and FFs (74%) in 2T tandem devices while only the one with poly-SiC_x CSPCs could achieve better current matching between the devices (19.5 mA/cm²). The EQE of the 2T tandem device (Figure 8b) shows that our bottom device can deliver 19.2 mA/cm², but that the top device limits the short-circuit current density of the stack to 17.8 mA/cm². By further optimizing the layer thickness and perovskite bandgap, the current generation of the two devices can be better matched and consequently, the efficiency of the 2T tandem devices can be further increased.

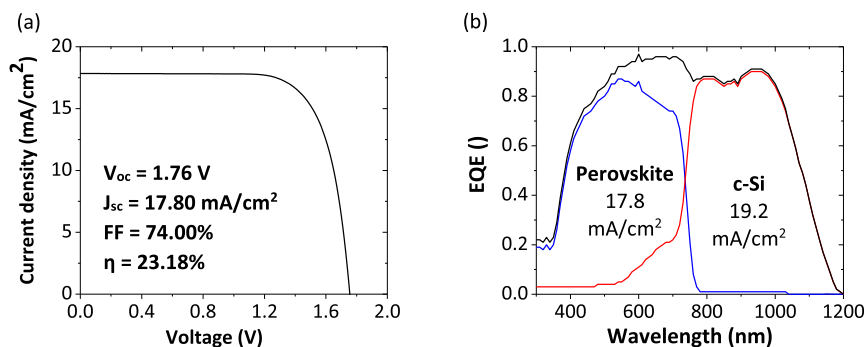


FIGURE 8 (a) Current density-voltage (*JV*) curve and (b) external quantum efficiency (EQE) curve of 2T perovskite/c-Si tandem solar cell with poly-SiO_x passivated c-Si bottom cell. The corresponding device structure is shown in Figure 1. The blue, red, and black curves represent EQE spectra of perovskite top cell, c-Si bottom cell, and tandem cell, respectively. The area covered by the blue line indicates the photo-current density generated by the perovskite top cell, whereas the area covered by the red line indicates the photo-current density generated by c-Si bottom cell. [Colour figure can be viewed at [wileyonlinelibrary.com](https://onlinelibrary.wiley.com/doi/10.1002/pip.3693)]

4 | CONCLUSIONS

In this study, we optimized n-type and p-type poly-SiO_x CSPCs on an ultra-thin thermally grown tunnelling SiO_x layer. We incorporated these into single junction c-Si solar cells, which were eventually used as bottom devices in 4T and 2T tandem devices. Good passivation quality was achieved for textured n-type poly-SiO_x ($iV_{oc} = 710$ mV). Using a two-step annealing process, the passivation quality of the textured p-type doped poly-SiO_x could be improved too ($iV_{oc} = 687$ mV). With the developed n-type and p-type poly-SiO_x CSPCs, we fabricated ~ 4 -cm² wide, screen-printed, a SST single junction c-Si solar cell with certified efficiency of 20.47% and FF > 80%. Likewise, a certified efficiency of 19.44% was obtained for a DST cell endowed poly-SiO_x CSPCs. This DST solar cell architecture is presented here for the first time and exhibits, without any dual anti-reflective coating, an active area $J_{sc} = 37.85$ mA/cm². This is in line with state-of-the-art FBC SHJ solar cells and other architectures based on high-thermal budget CSPCs.

We tested our c-Si solar cells in combination with a previously processed and certified semi-transparent 19.70% perovskite solar cell. The internally measured efficiencies of the 4T perovskite/c-Si tandem devices featuring SST and DST poly-SiO_x passivated c-Si bottom devices are 27.97% and 28.07%, respectively.

Based on the improved passivation quality of the textured p-type poly-SiO_x, we fabricated SST solar cell with flat n-type poly-SiO_x at the front side and textured p-type poly-SiO_x at the rear side with an efficiency of 16.79%. Integrating such a poly-SiO_x solar cell as bottom device with a p-i-n perovskite solar cell on top resulted in a 2T tandem device with an efficiency of 23.18%.

AUTHOR CONTRIBUTIONS

Manvika Singh: Conceptualization; analysis; experimental; investigation; visualization; writing—original draft; review and editing. **Kunal Datta:** Experimental; analysis; writing—review and editing. **Aswathy Amarnath:** Experimental. **Fabian Wagner:** Experimental. **Yifeng Zhao:** Writing—review and editing. **Guangtao Yang:** Writing—review and editing.

Andrea Bracesco: Experimental. **Nga Phung:** Experimental. **Dong Zhang:** Experimental; writing—review and editing. **Valerio Zardetto:** Experimental. **Mehrdad Najafi:** Experimental. **Sjoerd C. Veenstra:** Writing—review and editing. **Gianluca Coletti:** Writing—review and editing. **Mariadriana Creatore:** Writing—review and editing. **Martijn M. Weink:** Experimental. **René A. J. Janssen:** Writing—review and editing; supervision. **Arthur W. Weeber:** Funding acquisition; writing—review and editing. **Miro Zeman:** Funding acquisition. **Olindo Isabella:** Writing—review and editing; supervision; funding acquisition.

ACKNOWLEDGEMENTS

The authors acknowledge the NWO JSP III (680-91-011) program for the financial support. N.P. and M.C. acknowledge the financial support from “PERCpective,” specifically for the optimization of the NiO ALD process; M.N. and S.V. acknowledge the financial support from “HIPER XL”; these projects are part of the Top consortia for Knowledge and Innovation (TKI) Solar Energy program (TEUE119005 and 1921202, respectively) of the Ministry of Economic Affairs and Climate Affairs of The Netherlands. HIPER XL is also supported under the umbrella of SOLAR-ERA.NET Cofund by RVO. TNO (Netherlands Organization for Applied Scientific Research) acknowledges the financial support of Tandem PV Technology & Application program supported by Research and Cooperation Fund (SMO) from the Netherlands Ministry of Economic Affairs and Climate Policy.

REFERENCES

- Shockley W, Queisser HJ. Detailed balance limit of efficiency of p-n junction solar cells. *J Appl Phys*. 1961;32(3):510-519. doi:10.1063/1.1736034
- Andreani LC, Bozzola A, Kowalczewski P, Liscidini M, Redorici L. Silicon solar cells: toward the efficiency limits. *Adv Phys X*. 2019;4(1):1548305. doi:10.1080/23746149.2018.1548305
- Bush KA, Palmstrom AF, Yu ZJ, et al. 23.6%-Efficient monolithic perovskite/silicon tandem solar cells with improved stability. *Nat Energy*. 2017;2(4):17009. doi:10.1038/nenergy.2017.9
- Lal NN, Dkhissi Y, Li W, Hou Q, Cheng YB, Bach U. Perovskite tandem solar Cells. *Adv Energy Mater*. 2017;7(18):1602761. doi:10.1002/aenm.201602761

5. Sahli F, Werner J, Kamino BA, et al. Fully textured monolithic perovskite/silicon tandem solar cells with 25.2% power conversion efficiency. *Nat Mater.* 2018;17(9):820-826. doi:10.1038/s41563-018-0115-4
6. Oxford PV perovskite solar cell achieves 28% efficiency. 2018 Press Release by Oxford PV. <https://www.oxfordpv.com/news/oxford-pv-perovskite-solar-cell-achieves-28-efficiency>
7. Mazzarella L, Lin YH, Kirner S, et al. Infrared light management using a nanocrystalline silicon oxide interlayer in monolithic perovskite/silicon heterojunction tandem solar cells with efficiency above 25%. *Adv Energy Mater.* 2019;9(14):1803241. doi:10.1002/aenm.201803241
8. Nogay G, Sahli F, Werner J, et al. 25.1%-Efficient monolithic perovskite/silicon tandem solar cell based on a *p*-type monocrystalline textured silicon wafer and high-temperature passivating contacts. *ACS Energy Lett.* 2019;4(4):844-845. doi:10.1021/acsenergylett.9b00377
9. Zheng J, Mehrvarz H, Liao C, et al. Large-area 23%-efficient monolithic perovskite/heterojunction-silicon tandem solar cell with enhanced UV stability using down-shifting material. *ACS Energy Lett.* 2019;4(11):2623-2631. doi:10.1021/acsenergylett.9b01783
10. Köhnen E, Jošt M, Morales-Vilches AB, et al. Highly efficient monolithic perovskite silicon tandem solar cells: analyzing the influence of current mismatch on device performance. *Sustain Energy Fuels.* 2019; 3(8):1995-2005. doi:10.1039/C9SE00120D
11. Schmager R, Langenhorst M, Lehr J, Lemmer U, Richards BS, Paetzold UW. Methodology of energy yield modelling of perovskite-based multi-junction photovoltaics. *Opt Express.* 2019;27(8):A507-A523. doi:10.1364/OE.27.00A507
12. Liu Y, Li Y, Wu Y, et al. High-efficiency silicon heterojunction solar cells: materials, devices and applications. *Mater Sci Eng R Rep.* 2020; 142:100579. doi:10.1016/j.mser.2020.100579
13. Gharibzadeh S, Hossain IM, Fassel P, et al. 2D/3D heterostructure for semitransparent perovskite solar cells with engineered bandgap enables efficiencies exceeding 25% in four-terminal tandems with silicon and CIGS. *Adv Funct Mater.* 2020;30(19):1909919. doi:10.1002/adfm.201909919
14. Gota F, Langenhorst M, Schmager R, Lehr J, Paetzold UW. Energy yield advantages of three-terminal perovskite-silicon tandem photovoltaics. *Joule.* 2020;4(11):2387-2403. doi:10.1016/j.joule.2020.08.021
15. Oxford PV hits new world record for solar cell. 2020 Press Releases by Oxford PV. <https://www.oxfordpv.com/news/oxford-pv-hits-new-world-record-solar-cell>
16. Al-Ashouri A, Kohnen E, Li B, et al. Monolithic perovskite/silicon tandem solar cell with >29% efficiency by enhanced hole extraction. *Science.* 2020;370(6522):1300-1309. doi:10.1126/science.abd4016
17. Rohatgi A, Zhu K, Tong J, et al. 26.7% efficient 4-terminal perovskite-silicon tandem solar cell composed of a high-performance semitransparent perovskite cell and a doped poly-Si/SiO_x passivating contact silicon cell. *IEEE J Photovoltaics.* 2020;10(2):417-422. doi:10.1109/JPHOTOV.2019.2963564
18. Park HH, Kim J, Kim G, et al. Transparent electrodes consisting of a surface-treated buffer layer based on tungsten oxide for semitransparent perovskite solar cells and four-terminal tandem applications. *Small Methods.* 2020;4(5):2000074. doi:10.1002/smt.202000074
19. Subbiah AS, Isikgor FH, Howells CT, et al. High-performance perovskite single-junction and textured perovskite/silicon tandem solar cells via slot-die-coating. *ACS Energy Lett.* 2020;5(9):3034-3040. doi:10.1021/acsenergylett.0c01297
20. Xu J, Boyd CC, Zhengshan JY, et al. Triple-halide wide-band gap perovskites with suppressed phase segregation for efficient tandems. *Science.* 2020;367(6482):1097-1104. doi:10.1126/science.aaz5074
21. Chen B, Baek SW, Hou Y, et al. Enhanced optical path and electron diffusion length enable high-efficiency perovskite tandems. *Nat Commun.* 2020;11(1):1257. doi:10.1038/s41467-020-15077-3
22. Wang Z, Zhu X, Zuo S, et al. 27%-Efficiency four-terminal perovskite/silicon tandem solar cells by sandwiched gold nanomesh. *Adv Funct Mater.* 2020;30(4):1908298. doi:10.1002/adfm.201908298
23. Schulze PSC, Bett AJ, Bivour M, et al. 25.1% high-efficiency monolithic perovskite silicon tandem solar cell with a high bandgap perovskite absorber. *Sol RRL.* 2020;4(7):2000152. doi:10.1002/solr.202000152
24. World record: efficiency of perovskite silicon tandem solar cell jumps to 29.15 per cent. 2020 Press release by HZB. https://www.helmholtz-berlin.de/pubbin/news_seite?nid=21020;sprache=en
25. World record again at HZB: almost 30 % efficiency for next-generation tandem solar cells. 2021 Press Releases by HZB. https://www.helmholtz-berlin.de/pubbin/news_seite?nid=23248;sprache=en
26. Liu J, Aydin E, Yin J, et al. 28.2%-Efficient, outdoor-stable perovskite/silicon tandem solar cell. *Joule.* 2021;5(12):3169-3186. doi:10.1016/j.joule.2021.11.003
27. 2 new world records: perovskite-on-silicon-tandem solar cells. 2022 Press Releases by CSEM, EPFL. https://csem.cdn.prismic.io/csem/f46abbd1-6fe4-4554-9e0e-053152b390aa_CP2022-EPFL-worldrecord-EN.pdf
28. Wu Y, Zheng P, Peng J, et al. 27.6% perovskite/c-Si tandem solar cells using industrial fabricated TOPCon device. *Adv Energy Mater.* 2022; 12(27):2200821. doi:10.1002/aenm.202200821
29. Mariotti S, Jäger K, Diederich M, et al. Monolithic perovskite/silicon tandem solar cells fabricated using industrial *p*-type polycrystalline silicon on oxide/passivated emitter and rear cell silicon bottom cell technology. *Solar RRL.* 2022;6(4):2101066. doi:10.1002/solr.202101066
30. Ying Z, Yang Z, Zheng J, et al. Monolithic perovskite/black-silicon tandems based on tunnel oxide passivated contacts. *Joule.* 2022;6(11): 2644-2661. doi:10.1016/j.joule.2022.09.006
31. Yao Y, Hang P, Li B, et al. Phase-stable wide-bandgap perovskites for four-terminal perovskite/silicon tandem solar cells with over 30% efficiency. *Small.* 2022;18(38):2203319. doi:10.1002/sml.202203319
32. World record back at HZB: tandem solar cell achieves 32.5 percent efficiency. Press Release by HZB. https://www.helmholtz-berlin.de/pubbin/news_seite?nid=24348;sprache=en
33. Ko Y, Park HJ, Lee C, Kang Y, Jun Y. Recent progress in interconnection layers for hybrid photovoltaic tandems. *Adv Mater.* 2020;32(51): 2002196. doi:10.1002/adma.202002196
34. Li H, Zhang W. Perovskite tandem solar cells: from fundamentals to commercial deployment. *Chem Rev.* 2020;120(18):9835-9950. doi:10.1021/acs.chemrev.9b00780
35. Jst M, Kegelmann L, Korte L, Albrecht S. Monolithic perovskite tandem solar cells: a review of the present status and advanced characterization methods toward 30% efficiency. *Adv Mater.* 2020;10(26): 1904102.
36. Yang G, Ingenito A, Isabella O, Zeman M. IBC c-Si solar cells based on ion-implanted poly-silicon passivating contacts. *Sol Energy Mater Sol Cells.* 2016;158:84-90. doi:10.1016/j.solmat.2016.05.041
37. Haase F, Hollemann C, Schäfer S, et al. Laser contact openings for local poly-Si-metal contacts enabling 26.1%-efficient POLO-IBC solar cells. *Sol Energy Mater Sol Cells.* 2018;186:184-193. doi:10.1016/j.solmat.2018.06.020
38. Feldmann F, Reichel C, Müller R, Hermle M. The application of poly-Si/SiO_x contacts as passivated top/rear contacts in Si solar cells. *Sol Energy Mater Sol Cells.* 2017;159:265-271. doi:10.1016/j.solmat.2016.09.015
39. Richter A, Müller R, Benick J, et al. Design rules for high-efficiency both-sides-contacted silicon solar cells with balanced charge carrier transport and recombination losses. *Nat Energy.* 2021;6(4):429-438. doi:10.1038/s41560-021-00805-w

40. JinkoSolar's high-efficiency N-type monocrystalline silicon solar cell sets our new record with maximum conversion efficiency of 26.4%. Press Release by Jinko Solar. <https://www.jinkosolar.com/en/site/newsdetail/1827>
41. Ingenito A, Nogay G, Stuckelberger J, et al. Phosphorous-doped silicon carbide as front-side full-area passivating contact for double-side contacted c-Si solar cells. *IEEE J Photovolt*. 2019;9(2):346-354. doi:10.1109/JPHOTOV.2018.2886234
42. Nogay G, Ballif C, Ingenito A, et al. Crystalline silicon solar cells with coannealed electron- and hole-selective SiC_x passivating contacts. *IEEE J Photovolt*. 2018;8(6):1478-1485. doi:10.1109/JPHOTOV.2018.2866189
43. Stükelberger J, Nogay G, Wyss P, et al. Passivating electron contact based on highly crystalline nanostructured silicon oxide layers for silicon solar cells. *Sol Energy Mater sol Cells*. 2016;158:2-10. doi:10.1016/j.solmat.2016.06.040
44. Yang G, Guo P, Procel P, Weeber A, Isabella O, Zeman M. Polycrystalline silicon-oxide films as carrier-selective passivating contacts for c-Si solar cells. *Appl Phys Lett*. 2018;112(19):193904. doi:10.1063/1.5027547
45. Mewe A, Stodolny M, Anker J, et al. Full wafer size IBC cell with polysilicon passivating contacts. *AIP Conf Proc*. 2018;1999(1):040014.
46. van der Vossen R, Feldmann F, Moldovan A, Hermle M. Comparative study of differently grown tunnel oxides for p-type passivating contacts. *Energy Procedia*. 2017;124:448-454. doi:10.1016/j.egypro.2017.09.273
47. Lerch W, Kegel W, Niess J, Gelpelj J, Cristiano F. Scaling requires continuous innovation in thermal processing: low-temperature plasma oxidation. *ECS Trans*. 2012;45(6):151-161. doi:10.1149/1.3700948
48. Singh M, Santbergen R, Mazzarella L, et al. Optical characterization of poly-SiO_x and poly-SiC_x carrier-selective passivating contacts. *Sol Energy Mater sol Cells*. 2020;210:110507. doi:10.1016/j.solmat.2020.110507
49. Yang G, Han C, Procel P, et al. Oxygen-alloyed poly-Si passivating contacts for high-thermal budget c-Si heterojunction solar cells. *Prog Photovolt*. 2022;30(2):141-151. doi:10.1002/pip.3472
50. Messmer C, Goraya BS, Nold S, et al. The race for the best silicon bottom cell: efficiency and cost evaluation of perovskite-silicon tandem solar cells. *Prog Photovolt*. 2021;29(7):744-759. doi:10.1002/pip.3372
51. Nemeth B, Young DL, Page MR, et al. Polycrystalline silicon passivated tunneling contacts for high efficiency silicon solar cells. *J Mater Res*. 2016;31(6):671-681. doi:10.1557/jmr.2016.77
52. Polzin JI, Lange S, Richter S, et al. Temperature-induced stoichiometric changes in thermally grown interfacial oxide in tunnel-oxide passivating contacts. *Sol Energy Mater Sol Cells*. 2020;218:110713. doi:10.1016/j.solmat.2020.110713
53. Rui Z, Zeng Y, Guo X, et al. On the passivation mechanism of polysilicon and thin silicon oxide on crystal silicon wafers. *Sol Energy*. 2019;194:18-26. doi:10.1016/j.solener.2019.10.064
54. Temmler J, Polzin JI, Feldmann F, et al. Inline PECVD deposition of poly-Si-based tunnel oxide passivating contacts. *Phys Status Solidi (a)*. 2018;215(23):1800449. doi:10.1002/pssa.201800449
55. Holman ZC, Filipič M, Descoedres A, et al. Infrared light management in high-efficiency silicon heterojunction and rear-passivated solar cells. *J Appl Phys*. 2013;113(1):013107. doi:10.1063/1.4772975
56. Han C, Yang G, Montes A, et al. Realizing the potential of RF-sputtered hydrogenated fluorine-doped indium oxide as an electrode material for ultrathin SiO_x/poly-Si passivating contacts. *ACS Appl Energy Mater*. 2020;3(9):8606-8618. doi:10.1021/acsaem.0c01206
57. Qiu D, Duan W, Lambert A, et al. Effect of oxygen and hydrogen flow ratio on indium tin oxide films in rear-junction silicon heterojunction solar cells. *Sol Energy*. 2022;231:578-585. doi:10.1016/j.solener.2021.12.007
58. Sinton RA, Cuevas A. Contactless determination of current-voltage characteristics and minority-carrier lifetimes in semiconductors from quasi-steady-state photoconductance data. *Appl Phys Lett*. 1996;69(17):2510-2512. doi:10.1063/1.117723
59. Kerr MJ, Cuevas A, Sinton A. Generalized analysis of quasi-steady-state and transient decay open circuit voltage measurements. *J Appl Phys*. 2002;91(1):399-404. doi:10.1063/1.1416134
60. Phung N, Verheijen M, Todinova A, et al. Crystalline silicon solar cells with thin poly-SiO_x carrier-selective passivating contacts for perovskite/c-Si tandem applications. *ACS Appl Mater Interfaces*. 2022;14(1):2166-2176. doi:10.1021/acsaami.1c15860
61. Phung N, van Helvoirt C, Beyer W, et al. Effective hydrogenation of poly-Si passivating contacts by atomic layer deposited nickel oxide. *IEEE J Photovolt*. 2022;12(6):1377-1385. doi:10.1109/JPHOTOV.2022.3206895
62. al-Ashouri A, Magomedov A, Roß M, et al. Conformal monolayer contacts with lossless interfaces for perovskite single junction and monolithic tandem solar cell. *Energy Environ Sci*. 2019;12(11):3356-3369. doi:10.1039/C9EE02268F
63. Wang J, Zardetto V, Datta K, Zhang D, Wienk MM, Janssen RAJ. 16.8% monolithic all-perovskite triple junction solar cells via a universal two-step solution process. *Nat Commun*. 2020;11(1):1-10. doi:10.1038/s41467-020-19062-8
64. PhD research thesis by Kunal Datta 2022. <https://research.tue.nl/nl/persons/kunal-datta/publications/?type=%2Fdk%2Ffatira%2Fpure%2Fresearchoutput%2Fresearchoutputtypes%2Fthesis%2Fdoc1> (ISBN: 978-90-386-5558-1).
65. 30% yield achieved with four terminal perovskite silicon pv tandem cells. 2022 press Release by TNO. <https://www.tno.nl/nl/newsroom/2022/09/rendement-30-bereikt-vier-terminal/>
66. Zhang D, Najafi M, Zardetto V, et al. High efficiency 4-terminal perovskite/c-Si tandem cells. *Sol Energy Mater sol Cells*. 2018;188:1-5. doi:10.1016/j.solmat.2018.07.032
67. Najafi M, Zardetto V, Zhang D, et al. Highly efficient and stable semi-transparent p-i-n planar perovskite solar cells by atmospheric pressure spatial atomic layer deposited ZnO. *Solar RRL*. 2018;2(10):1800147. doi:10.1002/solr.201800147
68. Coletti G, Luxembourg S, Geerligs LJ, et al. Bifacial four-terminal perovskite/silicon tandem solar cells and modules. *ACS Energy Lett*. 2020;5(5):1676-1680. doi:10.1021/acseenergylett.0c00682
69. Werner J, Barraud L, Walter A, et al. Efficient near-infrared-transparent perovskite solar cells enabling direct comparison of 4-terminal and monolithic perovskite/silicon tandem cells. *ACS Energy Lett*. 2016;1(2):474-480. doi:10.1021/acseenergylett.6b00254
70. Yang G, Gram R, Procel P, et al. Will SiO_x-pinholes for SiO_x/poly-Si passivating contact enhance the passivation quality? *Sol Energy Mater sol Cells*. 2023;252:112200. doi:10.1016/j.solmat.2023.112200
71. Stuckelberger J, Yan D, Phang SP, et al. Pre-annealing for improved LPCVD deposited boron-doped poly-Si hole-selective contacts. *Sol Energy Mater sol Cells*. 2023;251:112123. doi:10.1016/j.solmat.2022.112123
72. Custer JS, Thompson MO, Jacobson DC, et al. Density of amorphous Si. *Appl Phys Lett*. 1994;64(4):437-439. doi:10.1063/1.111121
73. Datta K, Branco B, Zhao Y, et al. Efficient continuous light-driven electrochemical water splitting enabled by monolithic perovskite-silicon tandem photovoltaics. *Adv Mater Technol*. 2023;8(2):2201131. doi:10.1002/admt.202201131

How to cite this article: Singh M, Datta K, Amarnath A, et al. Crystalline silicon solar cells with thin poly-SiO_x carrier-selective passivating contacts for perovskite/c-Si tandem applications. *Prog Photovolt Res Appl*. 2023;1-11. doi:10.1002/pip.3693